Remote Sensing of Environment 114 (2010) 2594–2609

Contents lists available at ScienceDirect

Remote Sensing of Environment

journal homepage: www.elsevier.com/locate/rse

Development of a water clear of sea ice detection algorithm from enhanced SeaWinds/QuikSCAT and AMSR-E measurements

Stephen E.L. Howell [a,*], Chris Derksen [a], Adrienne Tivy [b]

[a] Climate Processes Section, Climate Research Division, Atmospheric Science and Technology Directorate, Environment Canada, Toronto, Ontario, Canada
[b] International Arctic Research Center, University of Alaska, Fairbanks, AK, USA

ARTICLE INFO

Article history:
Received 3 October 2009
Received in revised form 20 May 2010
Accepted 28 May 2010

Keywords:
Sea ice
Open water
QuikSCAT
AMSR-E
Algorithm development

ABSTRACT

We develop and evaluate water clear of sea ice (open water following ice cover) detection algorithms that make use of Scatterometer Image Reconstruction (SIR) SeaWinds/QuikSCAT (QuikSCAT) backscatter (σ°) and Advanced Microwave Scanning Radiometer for the Earth Observing System (AMSR-E) brightness temperature (T_B) measurements. Algorithm validation was performed within Canadian Arctic waters using the Canadian Ice Service Digital Archive (CISDA) ice charts, NASATeam ice concentration estimates, extended AVHRR Polar Pathfinder (APP-x) albedo data, RADARSAT-1 imagery, and MODIS imagery. Results indicate that the temporal evolution of QuikSCAT σ°, AMSR-E polarization ratio (PR18), and AMSR-E vertical spectral gradient ratio (GR3618) can detect water clear of sea ice events, however mean differences due to frequency dependent characteristics of the data (spatial resolution; sensitivity to open water) were apparent. All water clear of sea ice algorithms are in good agreement with the timing and clearing patterns given by the CISDA. The QuikSCAT algorithm provided a more representative ice edge and more details on the ice clearing process due to higher spatial resolution, however, transient clearing events were better represented by the AMSR-E PR(18) or (GR3618) algorithm. By exploiting the strengths of each sensor, we found that a QuikSCAT and AMSR-E fused algorithm provide improved open water area estimates by as much as 11%. The fusion of QuikSCAT and AMSR-E PR(18) yielded in the most spatially representative open water detection. The residual surface of the water clear of sea ice algorithms was found to provide another measure of the average September minimum pan-Arctic sea ice extent within 6% of the NASATeam algorithm estimates.

1. Introduction

The albedo of sea ice controls the absorption of shortwave solar radiation over a significant portion of the Earth's surface, thus strongly influences the state of the climate system. The detection of sea ice phenological events (e.g. melt onset, water clear of ice, and freeze onset) is important for understanding both regional and global climate processes because these events are associated with changes in shortwave albedo. A positive feedback is initiated when surface air temperatures increase over sea ice, driving a decrease in surface albedo leading to increased absorption of shortwave radiation that further accelerates the melt process (Curry et al., 1995). Early melt onset increases the total amount of shortwave radiation absorbed during the melt season (Perovich et al., 2007) amplifying the sea ice-albedo feedback mechanism that is suspected to account for part of the Arctic amplification observed in General Circulation Model simulations (Winton, 2006). Sea ice phenological events have also been shown to be sensitive indicators of climate variability and change. Increases in the length of the Arctic melt and open water seasons attributed to an earlier melt and later freeze (Stroeve et al., 2006) associated with the observed decreases in sea ice extent (Serreze et al., 2007) are reflective of these processes and the sensitive nature of sea ice in the climate system.

The significant contrast between the dielectric and subsequent emission properties of snow, ice, and water formulates the basis for sea ice phenological event detection from satellite measurements. Several algorithms exist to estimate the timing of melt and freeze onset over the Arctic from Scanning Multichannel Microwave Radiometer (SMMR) and Special Sensor Microwave/Imager (SSM/I) brightness temperatures (e.g. Drobot and Anderson, 2001; Belchansky et al., 2004; Markus et al., 2009). Unfortunately, the coarse spatial resolution of satellite passive microwave data makes resolving regions of the Canadian Arctic difficult because of numerous narrow channels. Active microwave observations from synthetic aperture radar (SAR) data have also been utilized to detect melt and freeze events (e.g. Winebrenner et al., 1994, 1996; Yackel et al., 2001; Kwok et al., 2003). SAR data does provide an improvement in spatial resolution but suffers from moderate temporal resolution and small areal coverage. As a result, in Canadian Arctic waters, melt and freeze detection algorithms have been developed from SeaWinds/QuikSCAT

* Corresponding author. Tel.: +1 419 739 5709.
E-mail address: Stephen.Howell@ec.gc.ca (S.E.L. Howell).

0034-4257/$ – see front matter.
doi:10.1016/j.rse.2010.05.027

(QuikSCAT) Scatterometer Image Reconstruction (SIR) backscatter measurements (e.g. Howell et al., 2008) that combine a high spatial resolution with complete daily coverage of the Arctic.

Considerable work has been done with respect to satellite melt and freeze detection but the break-up or open water transition period, which defines the period between melt onset and complete disappearance of sea ice has received less attention. Accurate estimates of the length of the open water period are important considering increases in Arctic air temperatures (Kaufman et al., 2009) have the potential to enhance the energy and moisture exchange over the ocean. Recently, Serreze et al. (2009) found the loss of summer sea ice attributed to an increase in the length of open water season has induced increases in autumn surface air temperatures over the Arctic. Interestingly, the dramatic loss of Arctic sea ice in 2007 (Stroeve et al., 2008) did not correspond to early melt onset dates (Markus et al., 2009) illustrating the need to independently retrieve these parameters. An open water event algorithm will also provide additional sea ice phenological information (melt duration season over seasonal first-year ice, the length of the open water season, and ice cover duration) by integrating timing estimates with previously established melt onset and freeze onset estimates (e.g. Howell et al., 2008; Markus et al., 2009).

Monitoring open water variability also has operational implications because of several major shipping routes including the Arctic Bridge from Russia to Hudson Bay, the Northern Sea Route, and the Northwest Passage through the Canadian Arctic Archipelago. Detecting and subsequently understanding open water variability is especially relevant within the Canadian Arctic Archipelago because its landfast nature dictates that sea ice movement only occurs when a route of open water is available (Melling, 2002). The Canadian Arctic Archipelago experienced its longest melt season length on record in 2008, yet the Western Parry Channel route through the Northwest Passage did not clear as it did in 2007 (Howell et al., 2009).

Previous studies have clearly shown that both active and passive microwave measurements can be used for detecting sea ice phenology although few algorithms have specifically explored time series water clear of sea ice detection or explored the utility of combining radiometer and scatterometer measurements. To our knowledge no algorithms exist to specifically provide water clear of sea ice estimates. For this work we i) evaluate the utility of time series SIR QuikSCAT backscatter (σ°) and AMSR-E brightness temperature (T_B) measurements for detecting water clear of sea ice events and ii) develop a water clear of sea ice timing algorithm for application within pan-Arctic waters. In addition, we also address the following questions: i) does a combination of QuikSCAT and AMSR-E improve open water detection? and ii) what combination of QuikSCAT σ° measurements and AMSR-E T_B frequencies provide the most representative detection?

2. Study area

We restrict our algorithm development and validation to the sea ice of Canada's Arctic because the various ice regimes within the region provide excellent opportunity to test the algorithm. Typically Canada's Arctic is divided into the Western Canadian Arctic, Eastern Canadian Arctic, and Hudson Bay (Fig. 1) and the sea ice regimes of the Canadian Arctic consists of the landfast regions of the CAA, the mobile pack ice of the Arctic Ocean found in the adjacent Canadian Basin, the marginal ice zone of southern Baffin Bay, and the seasonal ice of Hudson Bay. The sea ice matrix within the narrow channels of the Canadian Arctic Archipelago contains a mix of seasonal first-year ice

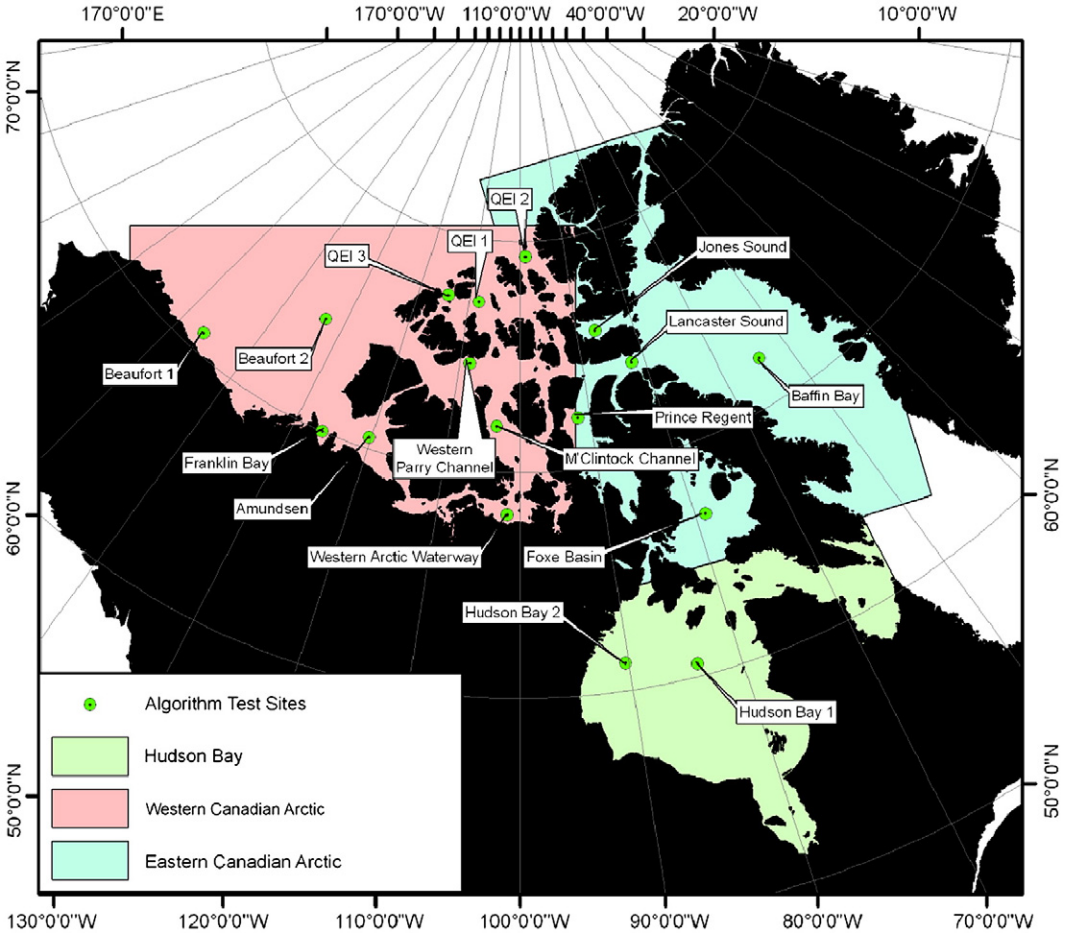

Fig. 1. Spatial boundaries of Hudson Bay, the Western Canadian Arctic, and the Eastern Canadian Arctic. The locations of the algorithm test sites are also shown.

(FYI) and multi-year ice (MYI) and so is likely the most difficult region to accurately capture open water events. Accurate detection within the Canadian Arctic Archipelago and the other ice regions that span the Canadian Arctic is no doubt representative enough for subsequent application to pan-Arctic open water detection.

Sea ice forms every winter in Canada Arctic waters and by mid-January all regions are completely ice covered and the only inter-annual variability in winter ice coverage is the extent of the ice edge south of Baffin Bay. On average, the first regions in the Canadian Arctic to clear of sea ice are the southeastern Beaufort Sea and northern Baffin Bay (CIS, 2002). In the southern Beaufort Sea flaw leads develop year round (Barber and Hanesiak 2004; Carmack et al., 2004) and in northern Baffin Bay the North Water Polynya forms every year (Dunbar, 1969). By mid-September when ice concentrations are at the annual minimum, Hudson Bay, Hudson Strait, the North Labrador Sea and the central region of the Western Arctic Waterway are typically completely ice free (CIS, 2002). In contrast, the Queen Elizabeth Islands, Western Parry Channel, and McClintock Channel often contain high concentrations of sea ice throughout the entire melt season because sea ice moves southeastward through the CAA often only resulting in temporary regions of open water.

3. Data

QuikSCAT SIR σ° measurements at both H and V polarizations were obtained from the SeaWinds scatterometer on board the NASA QuikSCAT satellite. The SeaWinds scatterometer is a dual-polarized real aperture radar operating at 13.4 GHz (Ku-band) providing normalized cross-section backscatter values at a fixed incident angle of 46° (H) and 54.1° (V) over a swath width of 1800 km with twice daily temporal resolution (i.e. daily ascending and descending passes). AMSR-E SIR T_B's measurements at both H and V polarizations for 18 and 36 GHz channels were obtained from the AMSR-E radiometer onboard the NASA Aqua satellite. The AMSR-E radiometer measures naturally upwelling microwave emission at an incidence angle of 55° over a swath width of 1445 km with a twice daily temporal resolution.

Both QuikSCAT and AMSR-E SIR products take advantage of spatial overlapping in σ° and T_B measurements taken at different times, thus increasing the sampling density in order to increase the spatial resolution (Long et al., 1993; Long and Daum, 1998; Gunn, 2007). However, it must be acknowledged that the limitations imposed on the SIR data are the sampling density, nulls data, the acceptable noise level, and the temporal stability of the study area (Long et al., 1993; Early and Long, 2001). AMSR-E SIR measurements are only available in one image product that exhibits a nominal spatial resolution of 8.6 km. QuikSCAT SIR measurements are available in two image products, eggs and slices with the nominal spatial resolution being 4.45 km for eggs and 2.25 km for slices. Although the slice products exhibit a higher spatial resolution, the lower resolution egg products contain less noise and are less sensitive to calibration errors, and hence are more appropriate for monitoring the thermodynamic evolution of snow and ice (e.g. Howell et al., 2005, 2008; Wang et al., 2008). Other than some potential coastal contamination, we suggest the aforementioned limitations of SIR products should be minimal with respect to open water detection because of the large dielectric and emission differences between ice and water.

The Canadian Ice Service Digital Archive (CISDA) ice charts were used to validate the water clear of sea ice event from time series SIR QuikSCAT and AMSR-E measurements. Digital ice charts are provided on a weekly basis by the Canadian Ice Service from 1968 to present for the Eastern and Western Canadian Arctic and from 1971 to present for Hudson Bay (Canadian Ice Service Digital Archive Documentation Series, 2007). The regional digital ice charts are derived weekly from the integration of data from a variety of sources including surface observations and aerial satellite reconnaissance and represent the best estimate of ice conditions based on all available information at the time (Canadian Ice Service Digital Archive Documentation Series, 2007). They are particularly beneficial for validating open water events because their primary data source has been RADARSAT-1 ScanSAR (100 m resolution) imagery since 1996. Both QuikSCAT and AMSR-E SIR products are independent of the CISDA. The weekly temporal resolution of the ice charts is such that they only provide a "snap-shot" of sea ice conditions on 1 specific day per week. While the ice charts provide an excellent validation source their temporal resolution dictates that an open water event could have occurred at most 6 days prior to the ice chart date. It is also possible that a transient open water event could have occurred during the week and sea ice quickly re-filled the open water gap. This issue underscores the problem with solely using the CISDA for open detection and the need for remotely sensed algorithms.

In order to provide more robust validation for our open detection algorithms we make use of several other datasets to complement the CISDA. Daily RADARSAT-1 ScanSAR imagery was acquired from the Canadian Ice Service to illustrate the water clear of sea ice processes at selected sites over the Canadian Arctic. RADARSAT-1 has a 24-day repeat cycle with a sun-synchronous, circular near polar orbit, transmitting and receiving at a frequency of 5.3 GHz (horizontally polarized). The onboard SAR is right looking and has 7 beam modes that image the Earth's surface at incident angles ranging from 20° to 49° off nadir. RADARSAT-1 ScanSAR images consist of a series of merged beams (Wide 1, 2, 3 and Standard Beams 5, 6 and 7) that are aggregated to produce a 460 km swath. The un-calibrated product is traditionally used by the Canadian Ice Service ice chart analysts and in order to be consistent with the CISDA no additional processing of the imagery was undertaken. Moderate Resolution Imaging Spectroradiometer (MODIS) quick look imagery was also acquired from the Geographic Information Network of Alaska (GINA) [http://www.gina.alaska.edu/]. The MODIS quick look imagery provided by GINA is a color-composite of Band 2 (250 m, 0.841 μm–0.876 μm) (Red), Band 3 (500 m, 0.459 μm–0.479 μm) (Green), and Band 31 (1000 m, 10.780 μm–11.280 μm) (Blue). Daily extended Advanced Very High Resolution Radiometer (AVHRR) Polar Pathfinder (APP-x; Wang and Key, 2005) surface broadband albedo data was also used to validate the open water event signal. The APP-x data is provided at a 25 km spatial resolution for regions 60°N with a root-mean square error for broadband albedo of 0.10 (Wang and Key, 2005). Finally, sea ice concentrations retrieved by the NASATeam algorithm (Cavalieri et al., 2008) when they reach 0 tenths were also used to validate water clear of sea ice estimates.

4. Algorithm development

A total of 17-test sites were selected over the Canadian Arctic (Fig. 1) to evaluate the response of QuikSCAT σ° and AMSR-E T_B measurements during the transition from an ice covered to an open water surface. These sites included: polynya and flaw-lead sites (Amundsen, Jones Sound, and Lancaster Sound), the MYI polar pack (Beaufort 1 and Beaufort 2), landfast FYI (Western Arctic Waterway and Prince Regent), non-landlocked FYI (Baffin Bay and Foxe Basin), landfast MYI (Queen Elizabeth Islands 1, Queen Elizabeth Islands 2, Queen Elizabeth Islands 3, M'Clintock Channel, and Western Parry Channel), and finally dynamic and tidally influenced seasonal FYI (Hudson Bay 1 and Hudson Bay 2). The QuikSCAT and AMSR-E measurement overlap begins in 2003 but APP-x albedo data is only available from 1982 to 2004. We choose 2004 as our primary test case year because of increased availability of valid daily APP-x albedo retrievals in 2004 compared to 2003.

4.1. Background

The strong dielectric permittivity (ε') contrast between snow ($\varepsilon' = 1.36$) and ice ($\varepsilon' = 3.15$) compared to water ($\varepsilon' = 80$) significantly influences both T_B and σ° values that allow for discrimination between geophysical states and surfaces (Ulaby et al., 1986). From a

T_B perspective, as air temperatures increases, liquid water begins to form between the snow grains and the snowpack becomes a source of microwave emission (Eppler et al., 1992). The result is an increase in surface emissivity and subsequent increases in T_B values signalling melt onset over both FYI and MYI (Anderson, 1997). As the melt processes continues, melt ponds form on the surface of the ice, the ability to discriminate FYI from MYI is lost, and T_B gradually decreases as radiometrically cold melt ponds replace radiometrically warmer sea ice (Grenfell and Lohanick, 1985). When complete breakup occurs and an open water surface dominates, T_B decreases significantly over FYI and over MYI it remains relatively stable due to the mix of melt ponds and snow/ice patches.

For our ASMR-E T_B water clear of sea ice detection algorithm we use the temporal evolution of the polarization (PR) and spectral gradient (GR) ratios defined by:

$$PR(18) = \frac{T_B(18V) - T_B(18H)}{T_B(18V) + T_B(18H)} \quad [1]$$

$$GR(3618) = \frac{T_B(36V) - T_B(18V)}{T_B(36V) + T_B(18V)}. \quad [2]$$

These indicators have been widely used in sea ice concentration algorithms because differences in horizontally and vertically polarized T_B's are large between sea ice (FYI and MYI) and open water (e.g. Cavalieri et al., 1984; Eppler et al., 1992; Comiso et al., 1997, 2003; Comiso and Parkinson, 2008).

Unlike T_B, the temporal evolution of σ° is different for FYI and MYI. For FYI, when the snow–ice interface temperature approaches −5 °C, brine volumes begin to increase which increases ε', and contributes to increased volume scattering (Barber and Nghiem, 1999). The result is high dielectric scattering centers which cause volume scattering, increasing σ° value which signals melt onset. The upturn in σ° over FYI surfaces continues as increases in the amount of high dielectric water in the snow cover results in greater amounts of snow surface and snow volume scattering (Drinkwater, 1989). Over MYI, melt onset is detected as liquid water increases within the snowpack that causes ε' to decrease as the larger amount volume scattering from the hummock layer is masked by snow surface scattering (Winebrenner et al., 1994). The σ° downturn over MYI surfaces continues as the lower snowcover scattering dominates over the higher air bubble volume scattering (Winebrenner et al., 1994). When melt ponds form on the surface, σ° follows a similar evolution over both FYI and MYI attributed to surface scattering. The relatively low ε' of the snow patches ($\varepsilon' = 1.99$ to 2.61) compared to the high ε' of melt ponds ($\varepsilon' = 65.81$) acts to maintain high σ° values (Barber and Yackel, 1999). As melt ponds begin to drain through brine drainage channels, sea holes and cracks in the ice, σ° will continue to decrease if an open water surface is reached (i.e. FYI) or will remain stable if the ice does not completely ablate (i.e. MYI).

For the QuikSCAT σ° water clear of sea ice algorithm we use the temporal evolution of the backscatter in H (σ°_H) and V (σ°_V) polarizations and active polarization ratio (APR) given by:

$$APR = \frac{\sigma^\circ_H - \sigma^\circ_V}{\sigma^\circ_H + \sigma^\circ_V}. \quad [3]$$

These indicators have successfully discriminated between sea ice types and open water using a threshold approach (e.g. Haarpaintner et al., 2004; Nghiem et al., 2006; Haarpainter and Spreen, 2007).

4.2. Single sensor approach

The transition from a sea ice surface to open water as detected by the QuikSCAT σ° is essentially marked by a steadily decreasing σ° following melt pond formation (Fig. 2). Despite this very noticeable change, several considerations must be taken into account to select an

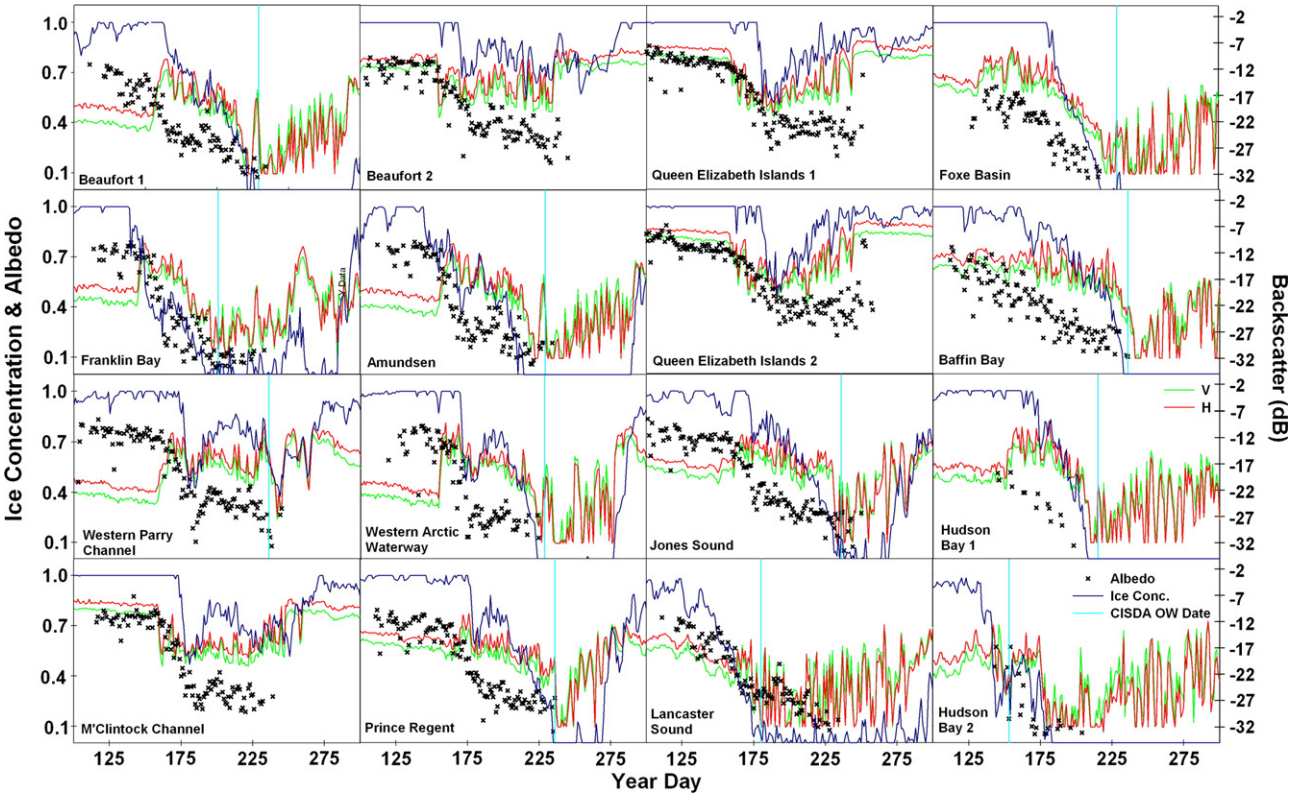

Fig. 2. Temporal evolution of QuikSCAT σ° at both H and V polarizations (right axis), APP-x albedo (left axis), and NASATeam ice concentration (left axis) for the Canadian Arctic algorithm test sites during 2004. The cyan solid vertical line represents open water (OW) as indicated by the Canadian Ice Service Digital Archive (CISDA) ice charts.

appropriate σ° threshold related to open water. For MYI, the first initial downturn from stable winter conditions signals melt onset, therefore the σ° detection threshold for open water must be low enough to avoid the initial melt onset signal. As the melt progresses, the snow patches act to maintain higher σ° than over a pure open water surface but as the melt ponds grow, σ° decreases. Therefore, the open water σ° threshold must also be low enough to avoid the low σ° values over a heavily melt ponded/snow patch surface which is typical over MYI sites (Fig. 2). This situation is less complicated over FYI because of higher σ° during the melt pond period, however FYI σ° values have been found to decrease down to almost −25 dB just prior to melt onset (Howell et al., 2005). This is likely attributed to ice lenses that can develop within the snowpack just prior to melt (Miller, 1981) that temporarily decrease σ° values.

Haarpainter and Spreen (2007) found an APR of −0.02 useful for discriminating between sea ice and ocean, detecting ice concentrations as low as 10%. While this APR threshold was particularly useful for FYI regions, false detection was apparent over MYI regions throughout the Canadian Arctic. For example, the APR time series for the Queen Elizabeth Islands 3 MYI site shows a distinct and strong increase near YD-180 (Fig. 3). This is coincident with decreases in surface albedo and decreases in the NASATeam ice concentration retrievals (Fig. 3) but examination of MODIS and RADARSAT-1 imagery during this time period reveals no open water is present (Fig. 4). Moreover, this region of the Queen Elizabeth Islands often remains landfast during the entire melt season (Melling, 2002). A heavily melt ponded surface is typically falsely detected as open water by thresholds between −0.02 and 0.05, underscoring the problem with using the APR for time series open water detection. Increasing the threshold to >0.06 was too extreme because it could not capture all open water events (not shown). Haarpaintner et al. (2004) suggested an H σ°<−23 dB is useful for distinguishing between ice and open ocean but noted that under higher wind speeds and where freeze–thaw events are occurring discrimination remained difficult. We found this threshold was still too low and employed a simultaneous σ° threshold of <−26 dB for both H and V polarizations that are within the calm open water ranges reported by Onstott (1992). For all 17-test sites, this simultaneous H and V<−26 dB threshold avoided false detection due to initial melt onset and extensive melt pond coverage over MYI and ice lenses development (Fig. 2). We suggest this threshold better identifies the first initial time of open water event and avoids false detection by a heavily melt ponded MYI surface compared to the APR and is more robust than the single H<−23 dB threshold. It should be noted that the σ° over water is very sensitive to wind speed increasing upwards of 10 dB between 1.5 and 20 ms^{-1} (Yueh et al., 1997; Yackel and Barber, 2000) and therefore our <−26 dB threshold is likely only applicable to calm wind conditions. We acknowledge that open water detection by our QuikSCAT thresholds may be late during rapid ice clearing events (high wind speeds) and/or in the marginal ice zones. In addition, this approach only detects the first appearance of open water and the re-fill of ice later is not be accounted for.

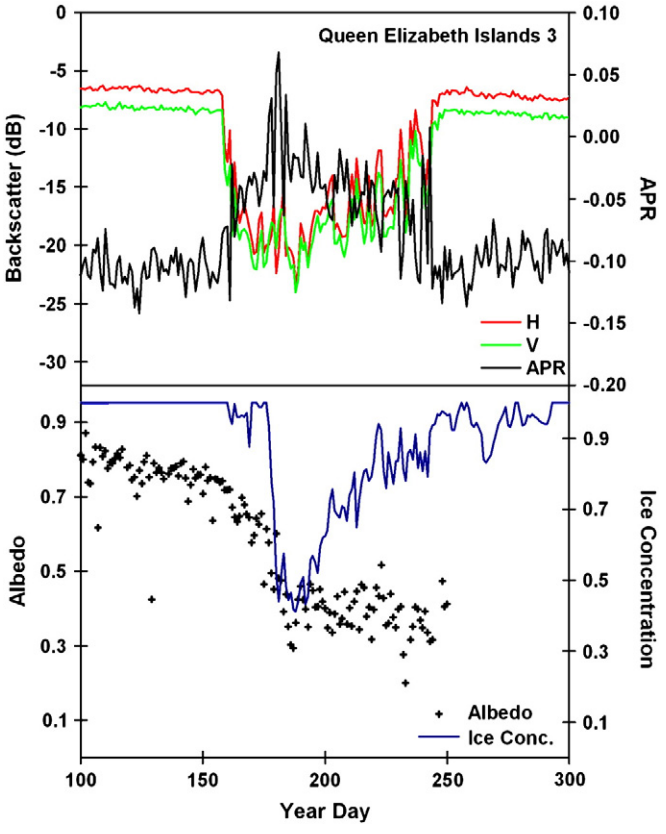

Fig. 3. Temporal evolution of QuikSCAT σ° at both H and V polarizations (top-left axis), active polarization ratio (APR; top-right axis), APP-x albedo (bottom-left axis), and NASATeam ice concentration (bottom left axis) for the Queen Elizabeth Islands 3 test site during 2004.

The transition from a sea ice surface to an open water surface can also by clearly identified by a sharp increase in both the AMSR-E PR (18) and GR(3618) time series (Fig. 5). Unlike σ° which is essentially a measure of surface scattering mechanisms, T_B is influenced by the physical temperature of the surface and emissivity, and care must be taken in selecting an appropriate open water threshold. Looking at the temporal evolution of the PR(18) and GR(3618) for the test sites indicates a significant T_B increase that corresponds to a decrease in surface albedo as the surface changes to open water (Fig. 5). The upturn is more pronounced over FYI than MYI but still occurs over both surfaces. As a result both AMSR-E PR(18) and GR(3618) thresholds must be high enough to avoid false detection over MYI melt ponds. Comiso et al. (2008) found an AMSR-E GR(3618) threshold of greater than 0.05 and an AMSR-E PR(18) of greater than ~0.25 corresponds to ice concentration of less than 10%. These values are similar to other previous studies (e.g. Cavalieri et al., 1984; Comiso et al., 1997). Because we are looking to provide the best estimate of the first appearance of open water with as little remnant sea ice as possible we have increased these AMSR-E GR(3618) and PR (18) thresholds to ≥0.07 and ≥0.26, respectively. As with the QuikSCAT algorithm, the AMSR-E GR(3618) and PR(18) algorithms only detect the first appearance of open water and re-fill of ice later is not accounted for.

4.3. Fused approach

The rationale behind our fused approaches was to take advantage of the strengths of each sensors in order to provide more temporally accurate and spatially representative date of the first occurrence of open water. This is especially important because the breakup process is not always purely thermodynamic and the role of dynamic processes needs to be accounted for. As the sea ice weakens, convergent ice motion may occur causing ridging and/or rafting. The latter is likely to exert negligible influence on σ° or T_B established open water threshold values but rapid breakup under the influence of winds that facilitates divergent sea ice motion maybe problematic for open water detection that relies solely on σ°. As winds generate rougher water surfaces (i.e. increasing σ°) the open water σ° threshold may not be reached as sea ice then immediately fills the open water gap. T_B values over the open ocean during extreme weather conditions such as heavy rain or large waves cause flooding over the ice do result in T_B fluctuations but these conditions are more problematic with respect to changes in σ°. It is also important to remember that SIR data is not just a 'drop in the bucket' but consists of multiple overpasses, hence wind roughening will likely cause more

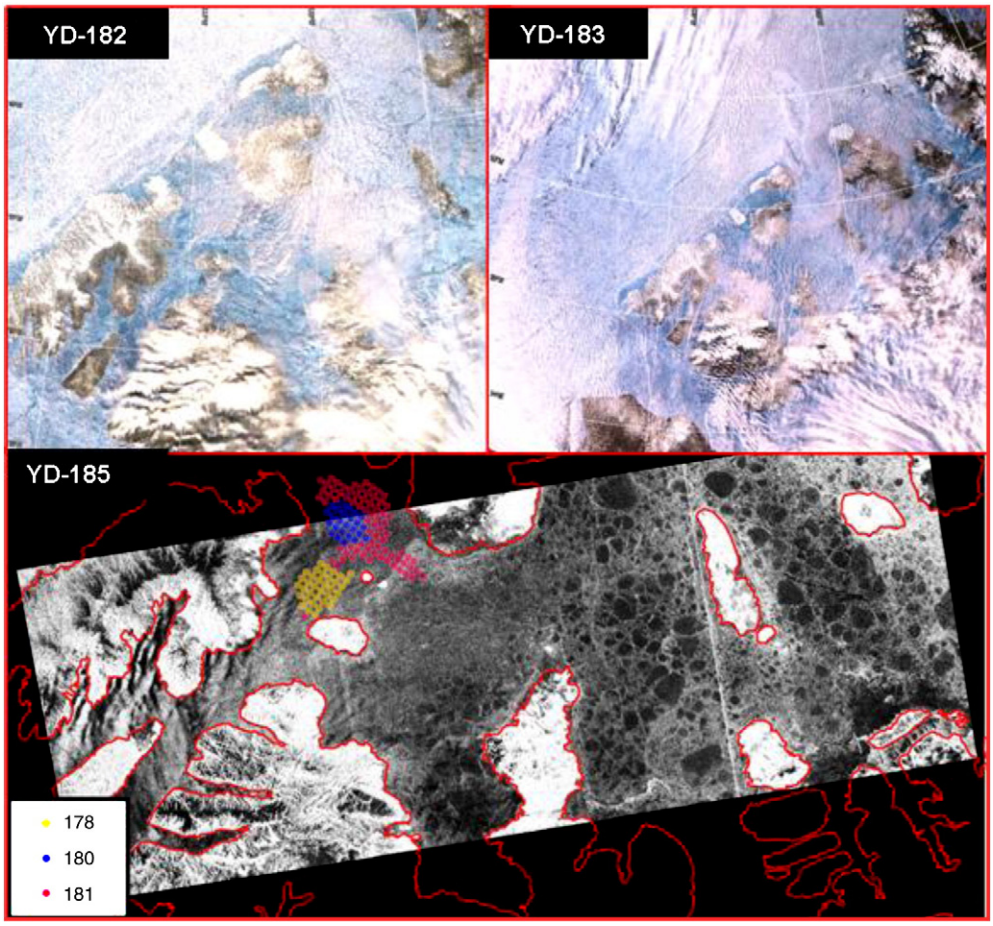

Fig. 4. MODIS imagery acquired over the Queen Elizabeth Islands 3 algorithm test site in 2004 (top panels). RADARSAT-1 ScanSAR image acquired Queen Elizabeth Islands 3 test site in 2004 overlaid with QuikSCAT active polar ratio (APR) open water detection dates (in YD) at a greater than 0.05 threshold (bottom panel).

SIR σ° fluctuations whereas SIR T_B values should remain more stable. Ultimately, the aforementioned transient events should exert less influence on T_B values yet, the increased sensitivity to liquid water content from the higher frequencies (i.e. 18 and 36 GHz) should also help detect these transient open water events. Despite QuikSCAT's sensitivity to surface conditions it exhibits a finer resolution by a factor of two compared to AMSR-E and therefore it is likely to better resolve spatial variability in open water.

Taking these factors into consideration we evaluate three combined open water algorithms: i) either AMSR-E PR(18) or AMSR-E GR(3618) thresholds must be reached, ii) either QuikSCAT H and V or AMSR-E PR(18) must be reached, and iii) either QuikSCAT H and V or AMSR-E GR(3618) thresholds must be reached. The thresholds outlined in the single sensor approach are the same. We have avoided an algorithm where both AMSR-E and QuikSCAT thresholds would have to be reached simultaneously because this is not separately exploiting the strengths of each sensor.

5. Results and discussion

5.1. Temporal comparison between single sensor open water detection algorithms

Table 1 shows the estimated open water dates from the single sensor algorithms as compared to the CISDA and the NASATeam ice concentration algorithm. For QuikSCAT, Beaufort 1, Franklin Bay, Western Arctic Waterway, Lancaster Sound, Jones Sound, Hudson Bay 1, and Hudson Bay 2 detected open water to have occurred 6 days earlier than indicated by the CISDA. For the Western Parry Channel, Prince Regent, and Baffin Bay, QuikSCAT detected open water at most 6 days later than indicated by the CISDA. All sites that did not reach a water surface (i.e. MYI sites that maintained a high σ°) as indicated by the CISDA were also not detected by our QuikSCAT open algorithm. Over these MYI sites, surface albedo's approached an open water value but the ε' of the ice and snow patches maintains a higher backscatter value above our −26 dB threshold (Fig. 2).

Transient test sites (i.e. Western Parry Channel, Lancaster Sound, Amundsen, Hudson Bay 2) are identified by significant QuikSCAT backscatter oscillations subsequent to the <−26 dB threshold coupled with NASATeam ice concentration oscillations (Fig. 2). For most transient test sites the first initial ice clearing event was correctly captured by QuikSCAT when compared to the CISDA (Fig. 2). Early QuikSCAT open water detection compared to the CISDA however did occur at the Amundsen (−11 days) and Foxe Basin (−10 days) test sites but this was likely initially missed by the CISDA (Table 2). There is a significant upturn in QuikSCAT backscatter that corresponds to increases in APP-x albedo at the Amundsen site circa YD-229 and for Foxe Basin there is an increase in NASATeam ice concentration suggesting clearing was followed by sea ice re-entering these test site pixels (Fig. 2).

Both the AMSR-E PR(18) and GR(3618) algorithms detected open water within 7 days of the CISDA for most test sites (Table 2). Open water was not detected at the MYI test sites in agreement with the CISDA. For the transient ice sites, oscillations in both the AMR-E PR(19) and GR(3618) time series are apparent following their respective open water thresholds but of lower magnitude compared to QuikSCAT (Fig. 5). As with QuikSCAT, the Foxe Basin and Amundsen test sites also experienced early detection with the AMSR-E PR(18) and GR(3618)

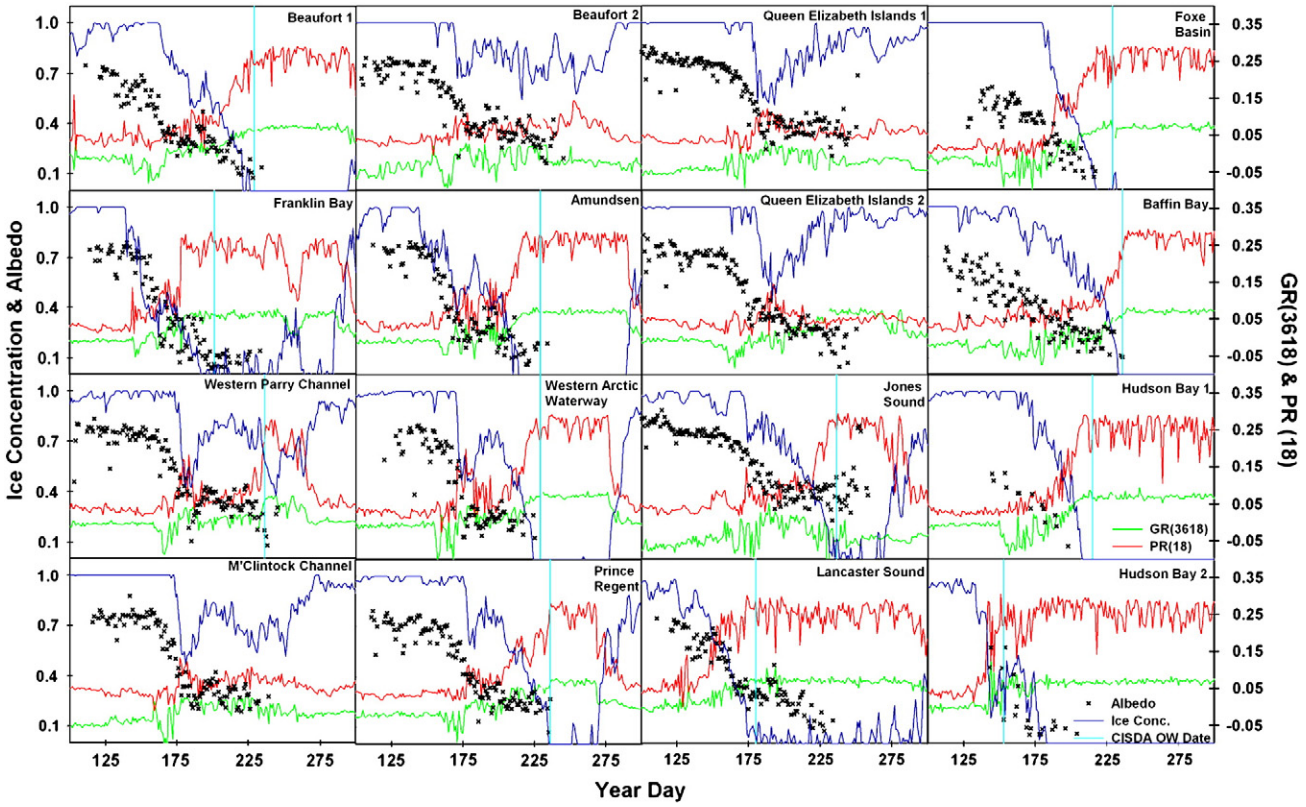

Fig. 5. Temporal evolution of AMSR-E PR(18) and GR(3816) ratios (left axis), APP-x albedo (left axis), and NASATeam ice concentration (left axis) for Canadian Arctic algorithm test sites during 2004. The cyan solid vertical line represents open water (OW) as indicated by the Canadian Ice Service Digital Archive (CISDA) ice charts.

algorithms. Additionally, the AMSR-E algorithms detected an early open water signal at the Franklin Bay test site that is likely a function of spatial resolution related to the floe edge of the Cape Bathurst Polynya. The Franklin Bay test site is located in landfast ice and the lower spatial resolution of AMSR-E (larger pixel area) detects open water earlier as the landfast ice edge degrades. The higher resolution of QuikSCAT (smaller pixel area) results in the open water of the polynya being detected later compared to AMSR-E. The time series of AMSR-E PR(18) and GR(3618) still finds high albedo and NASATeam ice concentration values after the open water thresholds are reached whereas the QuikSCAT threshold is more representative (Figs. 2 and 5).

In all test cases except Lancaster Sound and Hudson Bay 2, the NASATeam algorithm detects the first appearance of open water earlier than the CISDA (Fig. 2; Table 1). This is to be expected because it has long been known that passive microwave ice concentration retrievals underestimate actual ice concentration (e.g. Cavalieri et al., 1984). Agnew and Howell (2003) compared the CISDA to NASATeam ice concentrations and reported they underestimated by as much as 34% during the melt season. The NASATeam algorithm also missed the Western Parry Channel test site open water event as concentrations never fell below 40% (Fig. 2) and experienced considerable late detection over Hudson Bay 2 test site (Fig. 2). When comparing active and passive microwave melt onset algorithms Kwok et al. (2003) found the passive microwave algorithm to detected melt up to 15–20 days later over the Canadian Basin and the Eurasian Arctic. They suggested potential explanatory factors to be coarse resolution and that the backscatter response of radar is more sensitive to wetness than T_B. These factors are likely playing at role at the Western Parry Channel, Lancaster Sound, and Hudson Bay 2 test sites because they cleared quickly and then were immediately re-filled with ice.

Table 1
Comparison of open water (OW) dates at the 17-test sites as detected by the QuikSCAT and AMSR-E open water detection algorithms, the Canadian Ice Service Digital Archive, and the NASATeam algorithm for 2004. The date given by the CISDA is not exact and may have occurred 6 days earlier. The date given by the NASATeam algorithm is when the sea ice concentration reaches 0.

Site	CISDA	NASATeam	QuikSCAT H and V	AMSR-E PR(18)	AMSR-E GR(3618)
Beaufort 1	229	221	224	227	224
Beaufort 2	No OW	No OW	No OW	No OW	No OW
Franklin Bay	201	196	196	178	185
Western Arctic Waterway	229	210	224	225	222
Amundsen	229	214	218	216	216
Queen Elizabeth Islands 1	No OW	No OW	No OW	No OW	No OW
Queen Elizabeth Islands 2	No OW	No OW	No OW	No OW	No OW
Queen Elizabeth Islands 3	No OW	No OW	No OW	No OW	No OW
M'Clintock Channel	No OW	No OW	No OW	No OW	No OW
Western Parry Channel	236	No OW	242	237	239
Lancaster Sound	180	184	175	173	176
Jones Sound	236	235	232	230	231
Prince Regent	236	235	237	236	236
Foxe Basin	229	218	219	218	219
Baffin Bay	236	233	239	237	239
Hudson Bay 1	215	208	209	206	208
Hudson Bay 2	153	184	151	151	152

Table 2
Comparison of average first open water dates as detected by the single algorithms. Standard deviation in brackets.

Source	Western Canadian Arctic	Eastern Canadian Arctic	Hudson Bay
QuikSCAT H and V	211.4 (30.0)	190.4 (40.2)	196.6 (23.3)
AMSR-E PR(18)	215.5 (30.7)	186.2 (45.8)	190.7 (28.3)
AMSR-E GR(3618)	215.8 (30.2)	187.8 (45.2)	190.9 (29.1)
NASATeam	211.9 (25.8)	190.4 (42.1)	190.4 (20.8)

Evaluation at the test sites found that the QuikSCAT water clear of sea ice algorithm provided the closest open water timing estimates relative to the CISDA but this is only 2-day difference (on average) compared to the other algorithms. When all pixels are averaged over the regions of the Canadian Arctic, the difference in average water clear of sea ice dates between the algorithms only ranges between 1 and 5 days (Table 2). However, this bulk average tends to mask the inherent differences between the algorithms with respect to the nature of the clearing event as shown by the test cases. Therefore, we must look at differences between these algorithms spatially in order to determine the best detection approach.

5.2. Spatial comparison between single sensor open water algorithms

The spatial distribution of open water detection from the water clear of sea ice algorithms for 2004 is presented in Fig. 6. In the Western Canadian Arctic, all algorithms detected open water beginning first in the Cape Bathurst polynya and along the Beaufort Sea coast where the flaw-lead polynya system develops that is in agreement with the CISDA (Fig. 6; Fig. 7). Looking at daily RADARSAT-1 ScanSAR imagery from YD-139 to YD-157 also illustrates this process of polynya formation in agreement with QuikSCAT and AMSR-E algorithms (Fig. 8). For the Eastern Canadian Arctic, the North Water polynya region began to clear first in early spring and as the season progresses the open water area extended south past Lancaster Sound (Fig. 9). This process is captured extremely well by all water clear of sea ice algorithms (Fig. 8). For the landfast regions of the Canadian Arctic Archipelago, all algorithms correctly depicted clearing in the eastern region before the west as shown by the CISDA (Figs. 8, 10 and 11). Sea ice in the southern regions of Prince Regent survived the melt season of 2004 which was also captured by all algorithms (Figs. 8 and 10). All optimized water clear of sea ice algorithms also did not identify ice clearing in the western Queen Elizabeth Islands and Canadian Basin in agreement with the CISDA (Figs. 6 and 7). The NASATeam approach did experience some spurious false detection in the Queen Elizabeth Islands and the Canadian Basin (Fig. 6). For Hudson Bay the CISDA indicates that ice clearing begins in the early spring (YD-153) for the northwestern part of the bay, dynamic and thermodynamically driven clearing then proceeds from the northwest and the east with the ice along the southwest coast clearing last which is well represented by all algorithms (Figs. 6 and 10).

The overall spatial clearing patterns for the water clear of sea ice algorithms are in good agreement with the CISDA however, there are differences when inter-comparing the algorithms. Averaging the test sites finds that the QuikSCAT and both AMSR-E algorithms are slightly closer to the NASATeam estimate than CISDA, but the CISDA undoubtedly more accurate (i.e. the primary data source is RADARSAT-1 since 1996). Large and less dynamically active regions (e.g. central Hudson Bay and Baffin Bay) clearly experience earlier detection with the NASATeam approach (Fig. 6). These regions take longer to breakup and are heavily melt ponded which causes false detection for the NASATeam approach. The NASATeam approach experiences later detection in the Hudson Strait, the flaw-lead region of the Beaufort Sea, and north western Hudson Bay that range more than 2 weeks from the CISDA and the optimized algorithms (Fig. 6). These regions clear dynamically and represent a significant problem for the NASATeam algorithm likely attributed to the factors of spatial resolution and earlier detection by radar as suggested by Kwok et al. (2003).

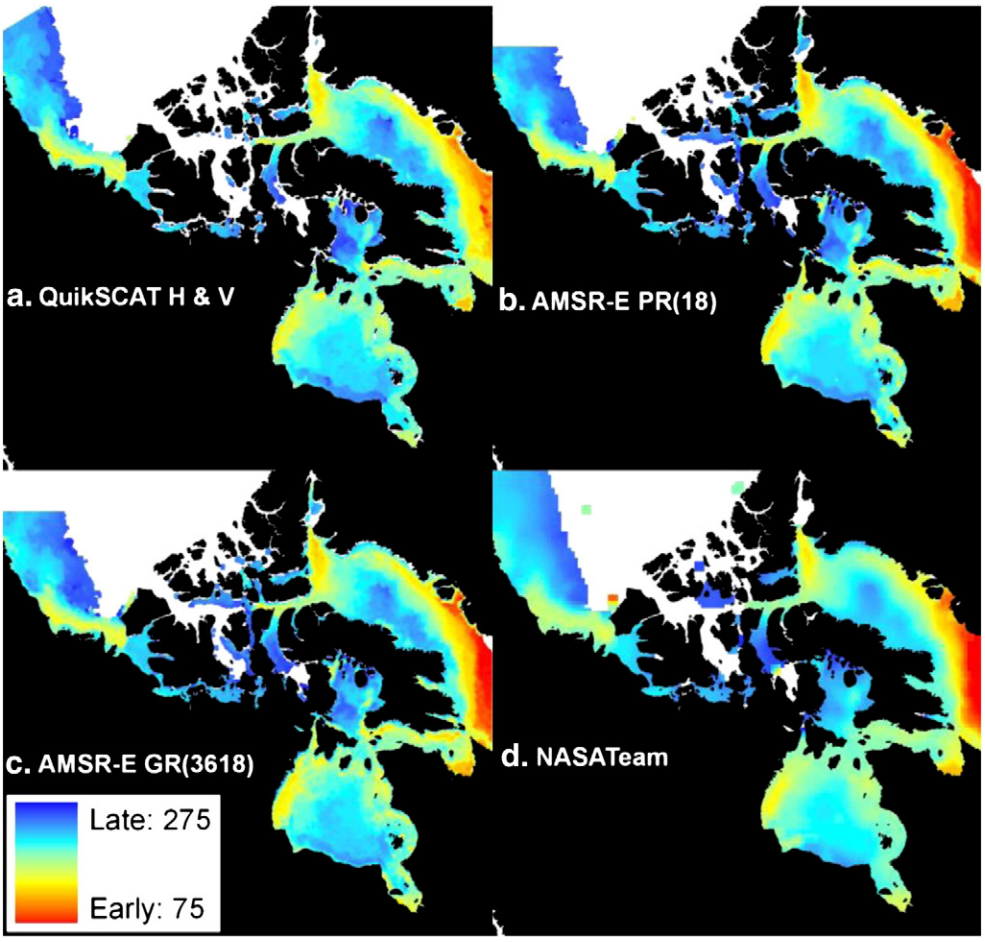

Fig. 6. Spatial distribution of first water clear of sea ice events over Canadian Arctic as detected by (a) QuikSCAT H and V σ° algorithm, (b) AMSR-E PR(18) algorithm, (c) AMSR-E GR (3618), and (d) NASATeam for 2004. Legend is year day.

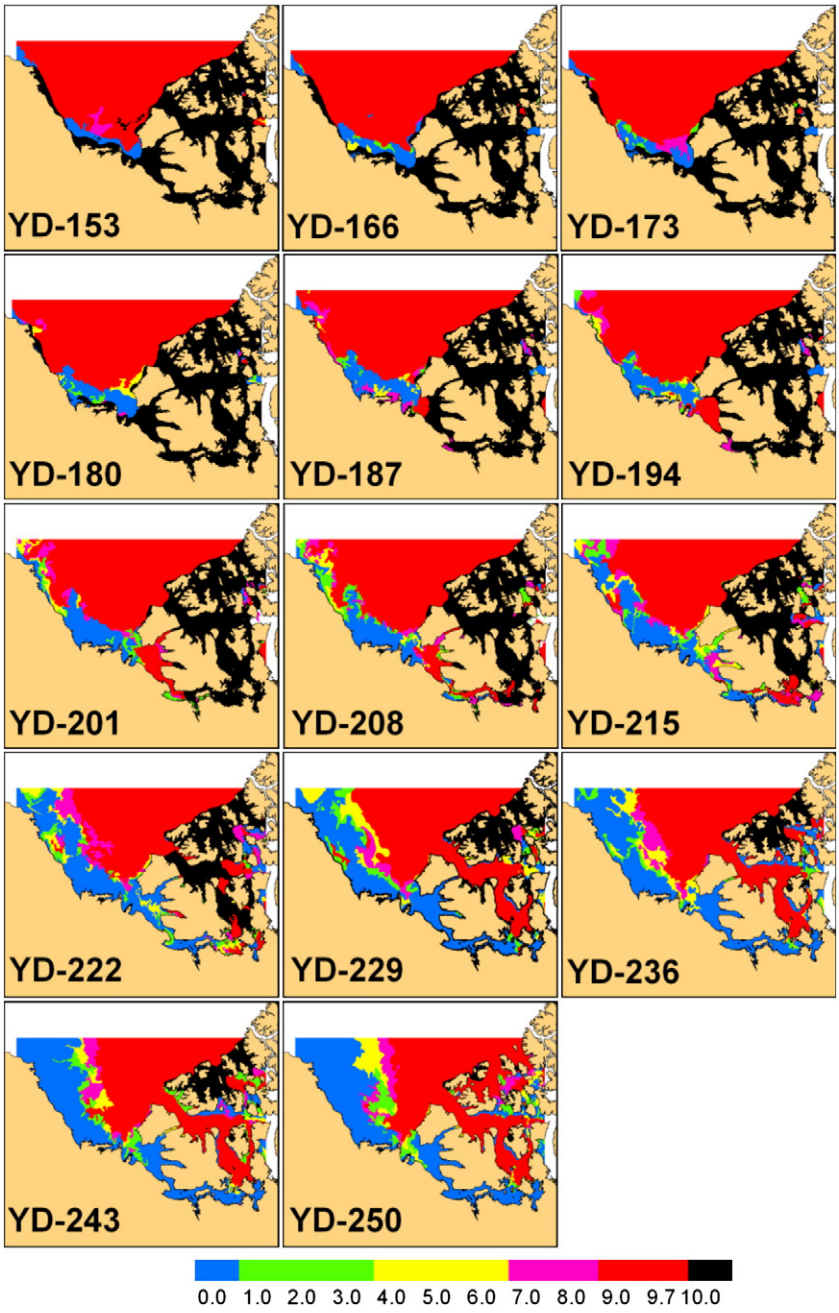

Fig. 7. Weekly spatial distribution of sea ice concentration in the Western Canadian Arctic for 2004 determined by the Canadian Ice Service Digital Archive ice charts. Legend is ice concentration in tenths.

Simply using the NASATeam approach to estimate the first occurrence of open water suffers from two problems. The first is a general tendency for the NASATeam approach to detect an earlier first open water date over the sea ice. The second is that in dynamically active clearing regions, late detection occurs. Since our algorithm is specifically optimized for time series open water detection, and because of the enhanced resolution of the SIR products these problematic factors are reduced. In addition, the NASATeam approach had difficultly detecting clearing in south regions of the Queen Elizabeth Islands, Nares Strait and the M'Clintock Channel compared to the optimized algorithms (Fig. 6). Therefore, we suggest the optimized time series open water algorithms are more appropriate to estimate the first date of open water compared to the NASATeam ice concentration retrievals.

Looking spatially at the QuikSCAT open water algorithm illustrates it had difficulty detecting the open water in the northern Western Parry Channel compared to the AMSR-E algorithms (Figs. 6 and 7). The QuikSCAT and AMSR-E algorithms detected the small regions of open water in the southwest region of the M'Clintock Channel but the sliver of open water on the western side of the M'Clintock Channel were only detected by the AMSR-E algorithms (Figs. 6 and 7). Examining RADARSAT-1 imagery from YD-226 to YD-237 further illustrates that clearing in these regions was captured in a more representative fashion by the AMSR-E algorithms (Fig. 11). This region is the main exit point for MYI from the Queen Elizabeth Islands as ice is continuously transported into the Western Parry Channel under the influence of winds during the melt season (Howell et al., 2009). Winds and continuous movement of MYI in this region are likely preventing the QuikSCAT threshold from being reached in certain regions of the Western Parry Channel. These transient surface events have less of an impact on SIR T_B values so the AMSR-E retrievals

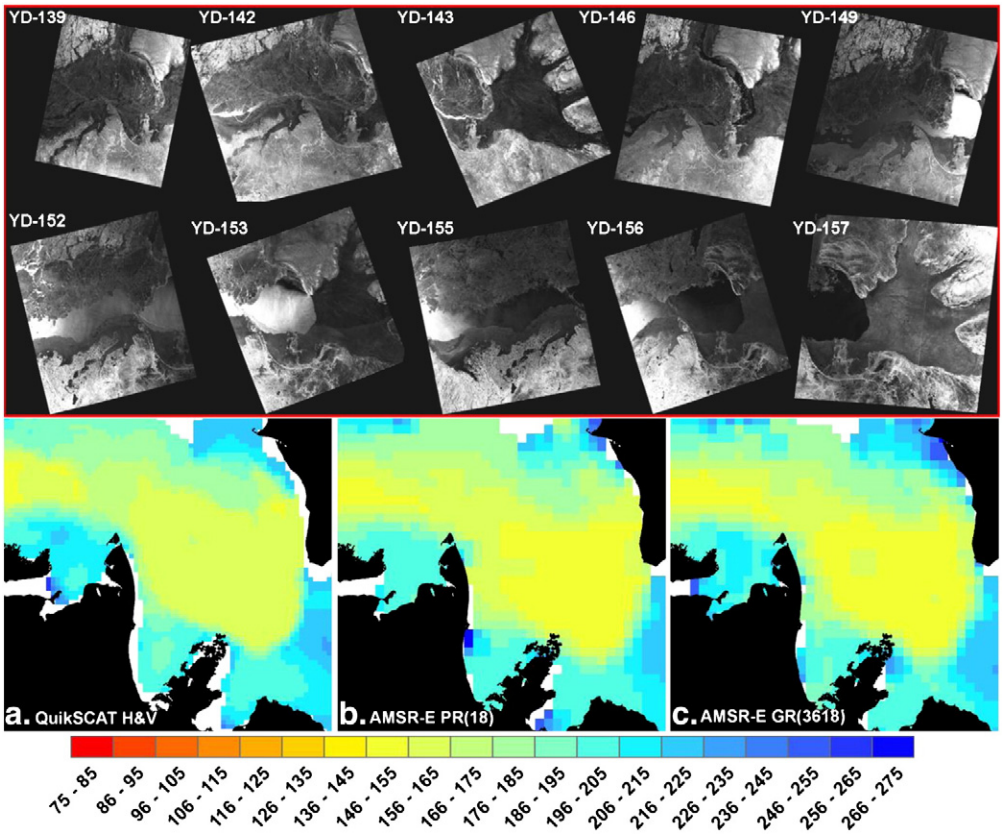

Fig. 8. Time series of 2004 RADARSAT-1 ScanSAR imagery from YD-139 to YD-157 in the Cape Bathurst Polynya region (top panels). Spatial distribution of the first date of open water over Canadian Arctic as detected by (a) QuikSCAT H and V σ° algorithm, (b) AMSR-E PR(18) algorithm, and (c) AMSR-E GR(3618) in the Cape Bathurst Polynya region for 2004 (bottom panels). Legend is year day.

provide the better estimate of open in the Western Parry Channel region compared to QuikSCAT.

Despite the higher resolution of QuikSCAT, the narrow and shallow channels of the Western Arctic Waterway are not fully represented because of land contamination (Fig. 6). Other bays and inlets throughout the Canadian Arctic also experience no detection by the open water QuikSCAT algorithm (Fig. 6). With respect to the AMSR-E algorithms, there is some improvement despite the slightly coarser resolution (Fig. 6). The effectiveness of the AMSR-E PR(18) and GR (3618) algorithms is also evident within the Western Parry Channel, the Baffin Inlet, and Nares Strait regions where ice clearing was not captured by the QuikSCAT algorithm (Fig. 6).

It seems apparent that within the Canadian Arctic, open water events in some regions are better resolved by σ°, but by T_B in other regions. A fused approach could therefore yield the most representative first date of open water estimate. We now explore the utility of fusing optimized open water algorithms by comparing them to the single sensor approach.

5.3. Fused open water detection algorithms

The spatial distribution of the fused water clear of sea ice algorithms is illustrated in Fig. 12. The fused QuikSCAT or AMSR-E algorithms provides a slightly more linear ice edge in the Beaufort Sea compared to QuikSCAT alone indicating that the lower resolution AMSR-E can mask the higher spatial resolution of QuikSCAT at the ice edge (Figs. 6 and 12). However, the spatial detail exhibited by the higher resolution QuikSCAT is preserved within large homogenous sea ice regions (e.g. Hudson Bay and Baffin Bay) (Fig. 12). The fusion of either AMSR-E PR(18) or GR(3618) with QuikSCAT certainly resolves transient events and increases open water detection within the bays and inlets of the Canadian Arctic (Fig. 12).

Table 3 shows a quantitative comparison of all algorithms at the week of maximum open water as indicated by the CISDA for the Eastern and Western Arctic from 2003 to 2008. Hudson Bay was omitted because it completely cleared during all seasons and all algorithms correctly detected this. On average, the single sensor algorithms underestimated CISDA maximum open water for all years by approximately -220×10^3 km^2 (−19%) in the Eastern Canadian Arctic and -151×10^3 km^2 (−24%) in the Western Canadian Arctic (Table 3). QuikSCAT was the lowest for the Canadian Western Arctic and AMSR-E PR(18) was the lowest for the Canadian Eastern Arctic (Table 3). Looking at the fused algorithms reveals that there is a marked increase in open water area compared to the single sensor algorithms (Table 3). On average, the fused AMSR-E PR(18) or GR(3618) underestimation for the Canadian Eastern and Western Arctic are less at -191×10^3 km^2 (−17%) and -122×10^3 km^2 (−20%), respectively, a ~3% improvement. QuikSCAT or AMSR-E PR(18) accounts for -154×10^3 km^2 (−14%) and -110×10^3 km^2 (−18%) for Eastern and Western Canadian Arctic, respectively a ~7% improvement. Finally the QuikSCAT or AMSR-E GR(3618) accounts for -112×10^3 km^2 (−10%) and -82×10^3 km^2 (−11%) for Eastern and Western Canadian Arctic, respectively, a ~11% improvement. Clearly, the fused algorithms provide increased open water area detection compared to single sensor approaches. This is encouraging as Yu et al. (2009) found that fusing QuikSCAT and AMSR-E improves sea ice classification within Canadian Arctic waters. It seems evident that the fusion of QuikSCAT or AMSR-E (3618) algorithm provides the increased open water detection compared to the CISDA.

Looking spatially at the QuikSCAT or AMSR-E GR(3618) fused algorithm illustrates that it detected more open water pixels along the coastline and in the shallow bays and inlets of the Canadian Arctic (i.e. Western Arctic Waterway, Lancaster Sound, Jones Sound, Baffin Bay and northwest Foxe Basin) and the Greenland coast (Fig. 12).

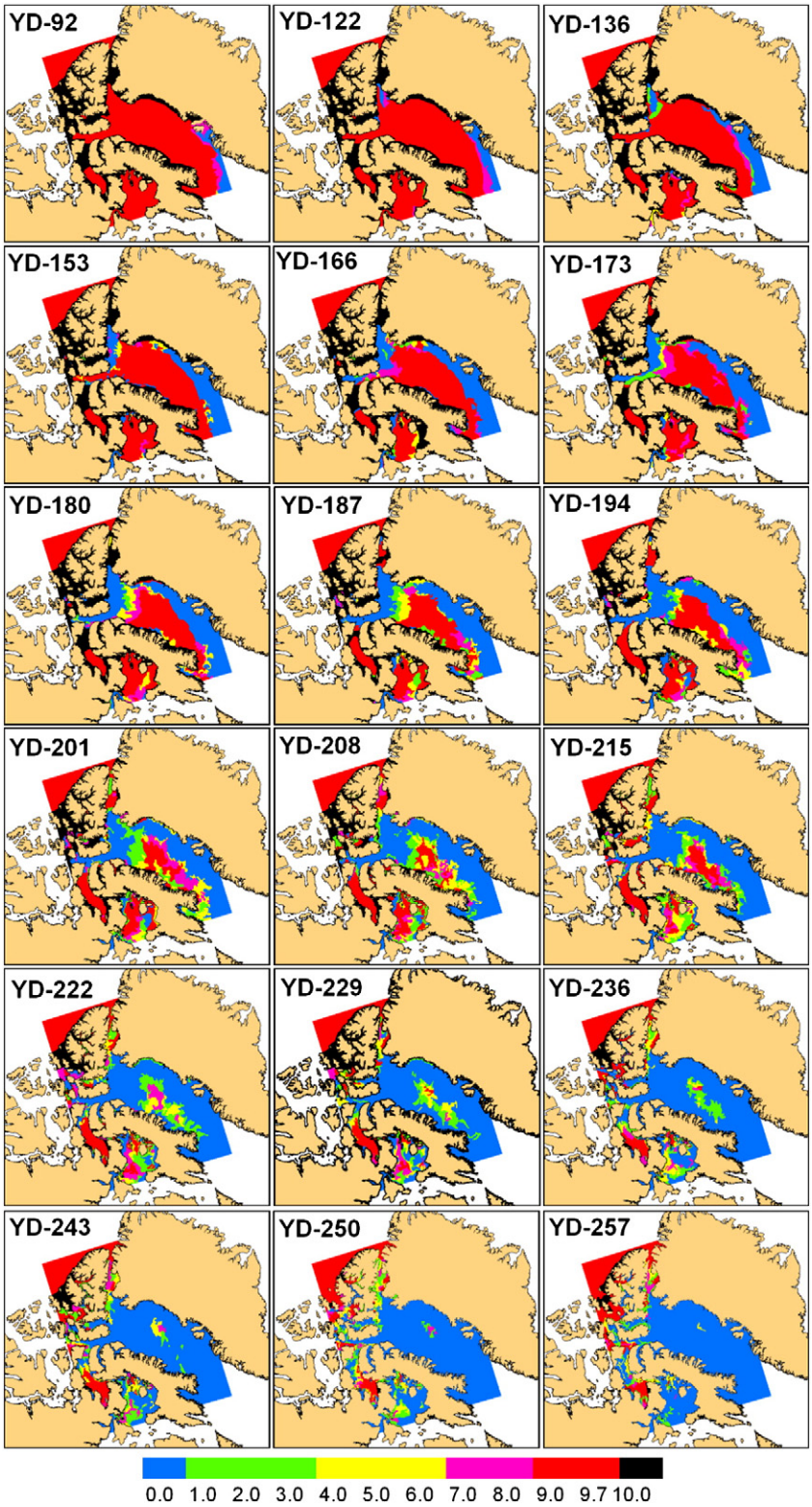

Fig. 9. Weekly spatial distribution of sea ice concentration in the Eastern Canadian Arctic for 2004 determined by the Canadian Ice Service Digital Archive ice charts. Legend is ice concentration in tenths.

However, when compared to the CISDA these pixels generally overestimate the open water date given by the CISDA. These false detections are likely the result of sensitivity of 37 GHz measurements to atmospheric water vapor late in the season (Mätzler, 1992; Markus et al., 2006; Tedesco and Wang, 2006). Examination of the QuikSCAT or AMSR-E PR(18) algorithm reveals that it does not capture as many pixels during maximum open water in the inlets and bays but the pixels it does resolve are in closer agreement with the CISDA (Fig. 12). While the combined QuikSCAT or AMSR-E GR(3616) algorithm may detect the most open water, the combined QuikSCAT or AMSR-E PR (18) algorithm provides a more representative estimate of the timing of open water.

The trade-off with the fused algorithms is a slightly less detailed ice edge compared to increased open water detection in the narrow

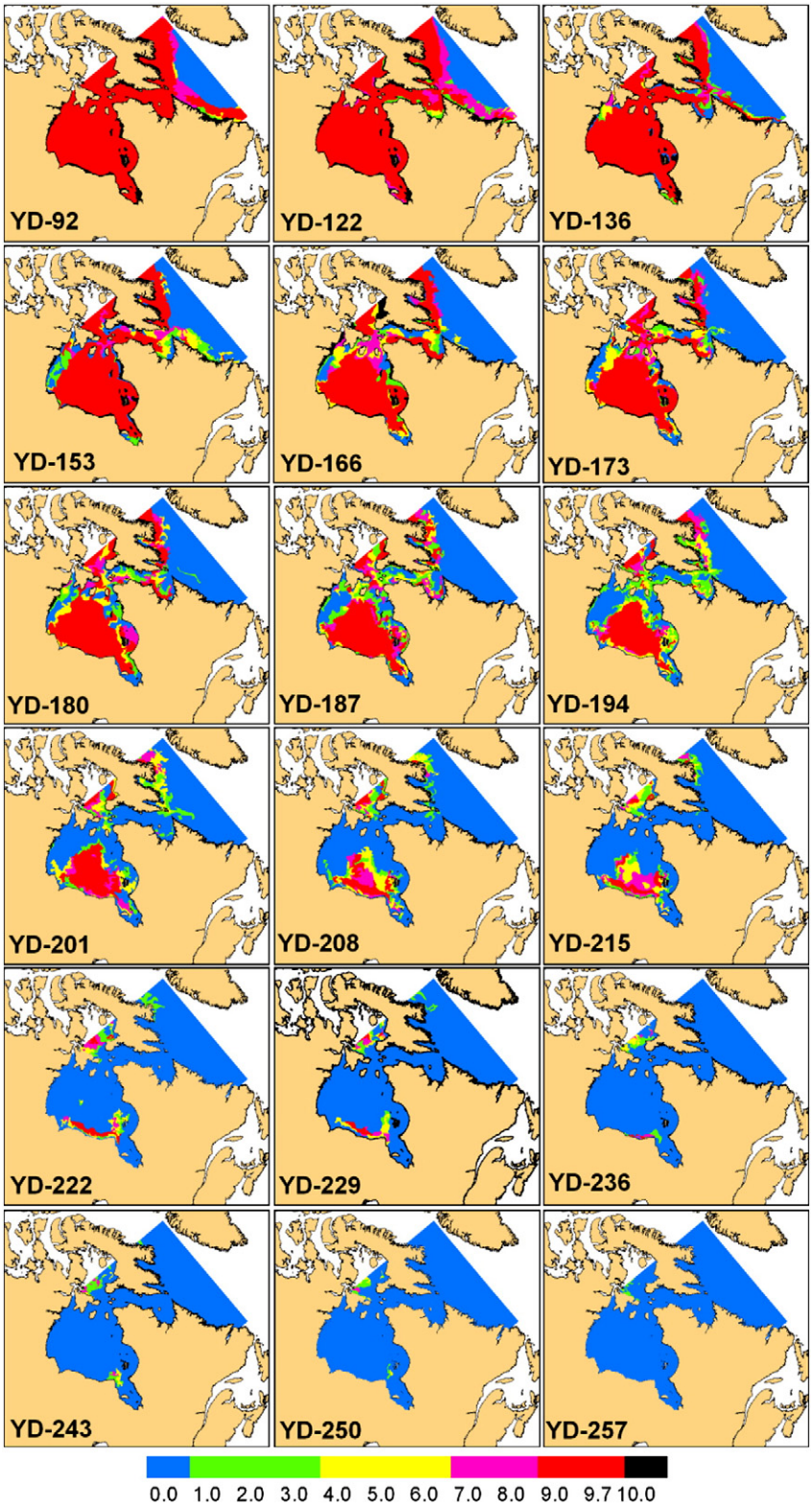

Fig. 10. Weekly spatial distribution of sea ice concentration in Hudson Bay for 2004 determined by the Canadian Ice Service Digital Archive ice charts. Legend is ice concentration in tenths.

channels and bays. However, our algorithms seeks to estimate the timing of open water, not resolve the ice-edge with great detail hence increased open water detection in the narrow channels and bays is more desirable. We now briefly examine the QuikSCAT or AMSR-E PR(18) water clear of sea ice algorithm applied to a pan-Arctic domain.

5.4. Pan-Arctic fused open water detection algorithm application

Fig. 13 illustrates the pan-Arctic water clear of sea ice dates determined by the fused QuikSCAT or AMSR-E PR(18) algorithm for 2003 to 2008, complemented by average September sea ice concentration estimates from SSM/I. Spatially, there is considerable

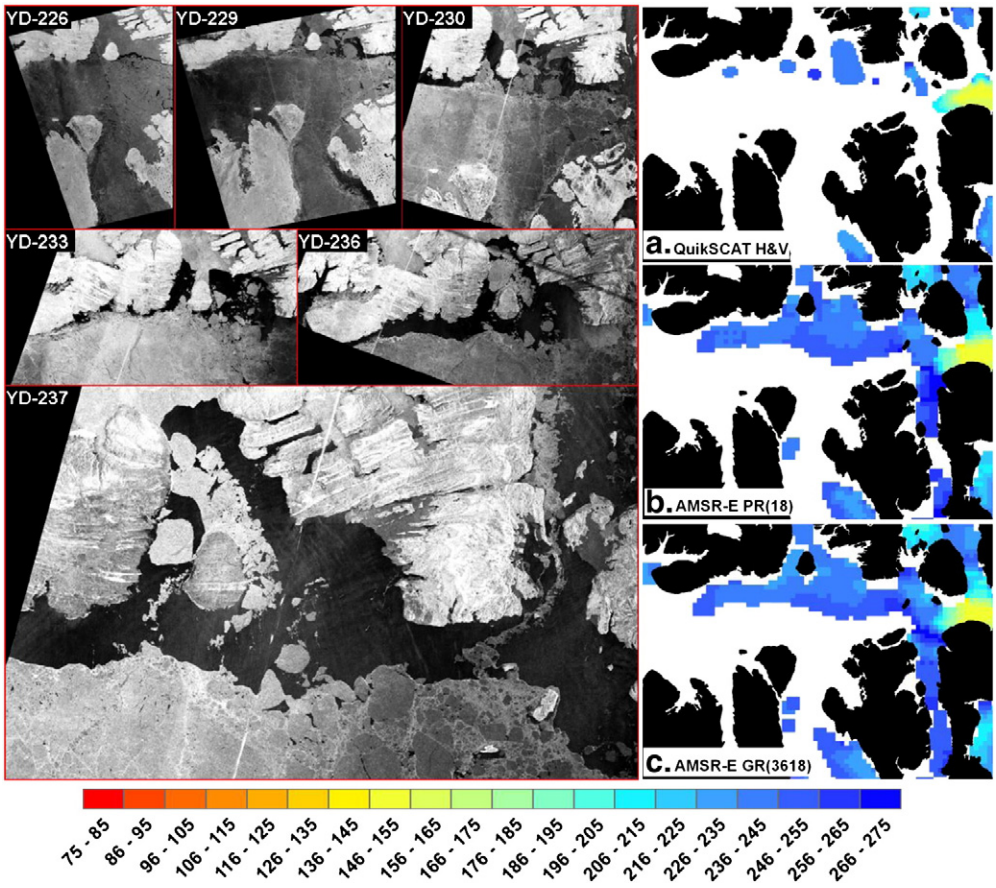

Fig. 11. Time series of 2004 RADARSAT-1 ScanSAR imagery from YD-226 to YD-237 in the Western Parry Channel region (left panels). Spatial distribution of the first date of open water over Canadian Arctic as detected by (a) QuikSCAT H and V σ° algorithm, (b) AMSR-E PR(18) algorithm, and (c) AMSR-E GR(3618) in the Western Parry Channel region for 2004 (right panels). Legend is year day.

inter-annual variability in the timing of open water dates from 2003 to 2008. Clearing initially begins in the Bering Sea and the Sea of Okhotsk then eventually progressing to the Chukchi Sea. This process can be seen occurring very early in 2007 which corresponded to an increased absorption of solar radiation (Perovich et al., 2008) and subsequent increased sea surface temperatures in the Chukchi Sea (Steele et al., 2008), both contributing the record low sea ice extent in 2007. While the open water in the Chukchi sea occurred later in 2008 (second lowest sea ice extent on record) there was considerably early clearing of the Beaufort Sea. For all years, the latest clearing dates correspond to the edge of the polar pack and the regions of the Canadian Arctic Archipelago. The sea ice regions that did not reach open water appear to be in good agreement with the minimum sea ice extent for the entire Arctic.

Table 4 provides the average September sea ice extent for pixels 60°N from the NASATeam algorithm as compared to the pixels 60°N for the QuikSCAT or AMSR PR(18) water clear of sea ice algorithm for 2003 to 2008. The results show the residual QuikSCAT or AMSR-E PR(18) algorithm surface is indeed in close agreement with the NASATeam algorithm accounting for only 6% more sea ice on average from 2003 to 2008. The dynamic nature of the MYI polar pack causes the ice to spread or contract, changing its extent over the melt season and therefore our residual open water surface does not perfectly mirror minimum sea ice extent. These differences are found predominately along the coastline (especially within the Canadian Arctic Archipelago) and along the ice edge where, ice concentration retrievals have been known to have problems because of coarse spatial resolution. In these problematic areas, it is simpler dielectrically to take an open water approach rather

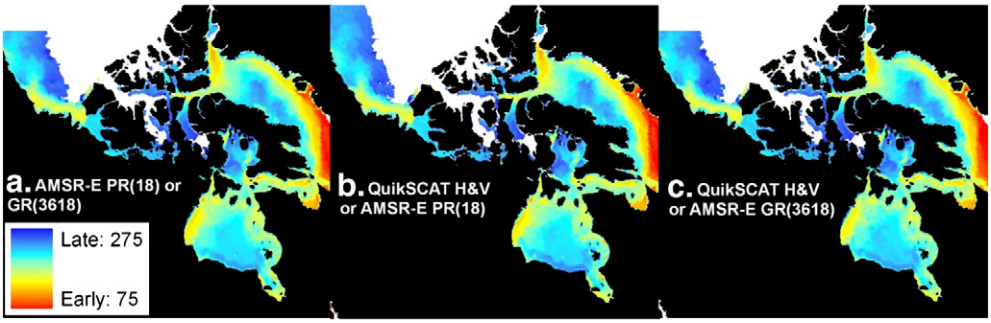

Fig. 12. Spatial distribution of first water clear of sea ice events over Canadian Arctic as detected by (a) AMSR-E PR(18) or GR(3618) fused algorithm, (b) QuikSCAT H and V σ° or AMSR-E PR(18) fused algorithm, and (c) QuikSCAT H and V σ° or AMSR-E GR(3618) fused algorithm for 2004. Legend is year day.

Table 3
Comparison between the open water area (km^2) detected by the QuikSCAT and AMSR-E open water algorithms and open water area (km^2) observed by Canadian Ice Service Digital Archive for the Eastern and Western Canadian Arctic from 2003 to 2008. The comparison was performed on date of maximum open water as determined by the Canadian Ice Service Digital Archive.

Year	CISDA	QuikSCAT H and V	AMSR-E PR(18)	AMSR-E GR(3618)	AMSR-E PR (18) or GR(3618)	QuikSCAT H and V or AMSR-E PR(18)	QuikSCAT H and V or AMSR-E GR(3618)
Western Canadian Arctic							
2003	455×10^3	332×10^3	348×10^3	367×10^3	370×10^3	378×10^3	402×10^3
2004	579×10^3	430×10^3	446×10^3	463×10^3	468×10^3	484×10^3	506×10^3
2005	421×10^3	241×10^3	270×10^3	287×10^3	294×10^3	296×10^3	319×10^3
2006	527×10^3	348×10^3	378×10^3	394×10^3	404×10^3	414×10^3	437×10^3
2007	841×10^3	599×10^3	676×10^3	691×10^3	701×10^3	708×10^3	756×10^3
2008	884×10^3	702×10^3	707×10^3	732×10^3	738×10^3	766×10^3	797×10^3
Average	618×10^3	442×10^3	471×10^3	489×10^3	496×10^3	508×10^3	536×10^3
Eastern Canadian Arctic							
2003	108×10^4	898×10^3	883×10^3	920×10^3	924×10^3	960×10^3	100×10^4
2004	104×10^4	846×10^3	835×10^3	864×10^3	869×10^3	906×10^3	940×10^3
2005	119×10^4	929×10^3	930×10^3	965×10^3	973×10^3	101×10^4	106×10^4
2006	119×10^4	950×10^3	945×10^3	987×10^3	992×10^3	103×10^4	108×10^4
2007	117×10^4	922×10^3	925×10^3	958×10^3	968×10^3	101×10^4	105×10^4
2008	116×10^4	905×10^3	911×10^3	949×10^3	959×10^3	992×10^3	104×10^4
Average	114×10^4	908×10^3	904×10^3	940×10^3	948×10^3	985×10^3	103×10^4

than estimating sea ice concentration. The higher resolution of the SIR measurements used in our open water algorithm certainly helps resolve the regions of the Canadian Arctic Archipelago (Fig. 13). An excellent example of this is how a 'sliver' of open water remains through the Western Parry Channel during 2008 (Fig. 13). This is a direct result of MYI continuously flowing across the channel during the melt season, preventing the Northwest Passage from opening in 2008 (Howell et al., 2009). The 'hole' of open water within the polar pack during 2006 is also particularly well resolved by our open water algorithm (Fig. 13).

6. Conclusions

The dielectric dissimilarities between ice and ocean dictate that open water thresholds from either QuikSCAT σ° or AMSR-E T_B's can be used to detect the timing of open water events. We developed water clear of sea ice algorithms from QuikSCAT σ° using both H and V polarizations and AMSR-E T_B's using the PR(18) and GR(3618) ratios and validated them within the Canadian Arctic using the CISDA, the NASATeam sea ice concentration algorithm, APP-x albedo data, RADARSAT-1 imagery and MODIS imagery. The optimized open water detection thresholds and enhanced resolution SIR products suggest the QuikSCAT and AMSR-E algorithm is more appropriate to detect the first occurrence of open water compared to the NASATeam algorithm.

Based on our test sites, the QuikSCAT open water thresholds provided the closest estimate to that of the CISDA but when open water surfaces were generated over the Canadian Arctic, inherent open water spatially variability became apparent. Individually, the QuikSCAT water clear of sea ice algorithm provided a more representative ice edge and provides more details on the clearing process due to higher spatial resolution, however, transient clearing events are better represented by the AMSR-E PR(18) or (GR3618) algorithm. Since open water events were sometimes better resolved by σ° and sometimes by T_B, we developed and evaluated several fused QuikSCAT and AMSR-E open water algorithms. These fused algorithms improved open water area detection by as much as 11%

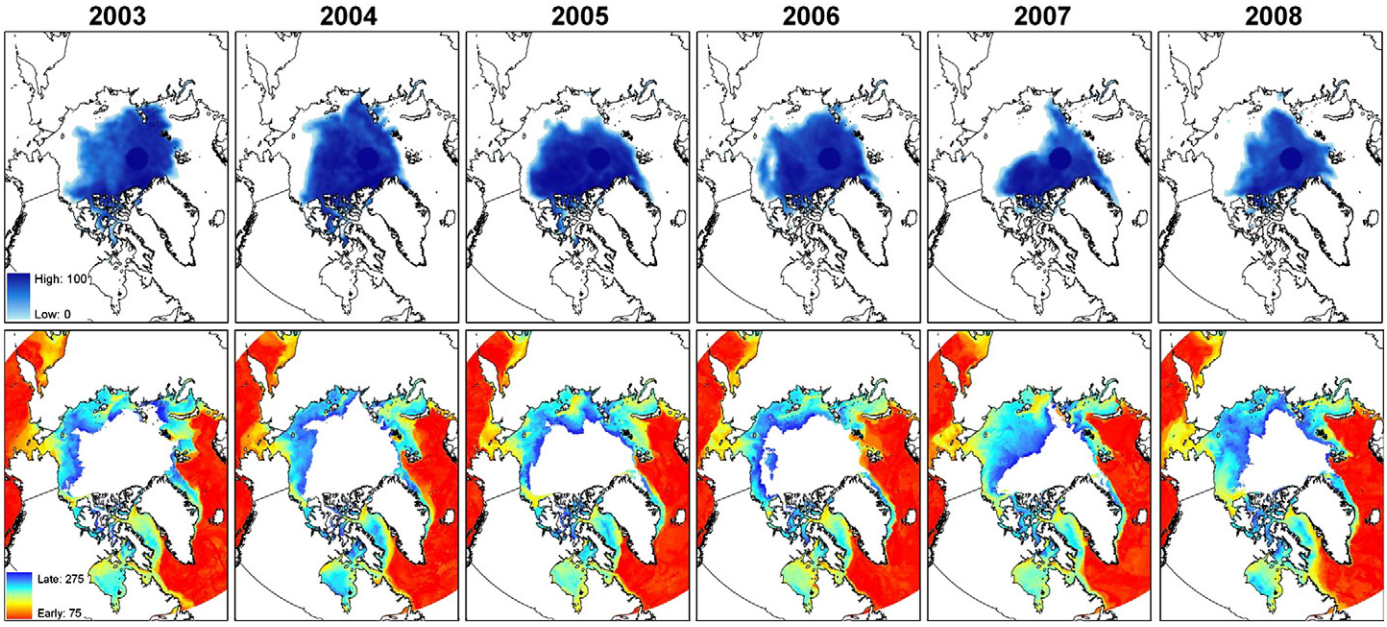

Fig. 13. Average September sea ice concentration (in percent) estimates determined by the NASATeam algorithm for 2003 to 2008 (top panels). Spatial distribution of pan-Arctic first water clear of sea ice dates (in YD) determined by the QuikSCAT H and V σ° or AMSR-E PR(18) fused algorithm for 2003 to 2008 (bottom panels).

Table 4
Comparison of NASATeam derived average September sea ice extent (km^2) and the fused QuikSCAT H and V or AMSR-E PR(18) open water algorithm residual area greater than 60°N from 2003 to 2008.

Year	NASATeam	QuikSCAT H and V or AMSR-E PR(18)
2003	6.22×10^6	6.42×10^6
2004	6.12×10^6	6.46×10^6
2005	5.63×10^6	5.89×10^6
2006	6.00×10^6	6.08×10^6
2007	4.37×10^6	4.83×10^6
2008	4.57×10^6	5.22×10^6

percent. Specifically, combined QuikSCAT or AMSR-E GR(3618) GHz was found to detect the most open water timing events but the combined QuikSCAT or AMSR-E PR (18) algorithm provided a more representative open water timing detection compared to the CISDA.

The combined QuikSCAT or AMSR-E PR(18) open water algorithm was successfully applied over the pan-Arctic domain to not only provide spatial first open water date estimates that complement ice concentration retrievals but also provide a measure of the minimum MYI extent reached over the season. On average from 2003 to 2008 we found the residual open water surface was within 6% of the average September sea ice extent as determined by the NASATeam algorithm. Although the fused algorithms provide improved estimates of the timing of open water events, there is still merit in the single sensor approaches. In order to examine longer term variability, the PR(18) and GR(3618) approaches are the only suitable choice for the full SMMR-SSM/I passive microwave record (1979 to present). QuikSCAT can provide 10 years of SIR open water estimates but only single sensor AMSR-E SIR measurements will be available in the immediate future as QuikSCAT reached the end of its lifespan in 2009. Considering the Arctic is advancing toward a summertime sea ice free regime, estimates of the timing of sea ice phonological events at both the regional and pan-Arctic scale represent important information to better understand this transition and the responsible processes.

Acknowledgments

This research was supported by a Visiting Fellowship to S. Howell. We would like to thank D. Long (Brigham Young University) for the SIR QuikSCAT and AMSR-E data products. We also would like to thank the three anonymous reviewers who greatly improved this manuscript.

References

Agnew, T., & Howell, S. (2003). The use of operational ice charts for evaluating passive microwave ice concentration data. *Atmos. Ocean*, *41*(4), 317−331. doi:10.3137/ao.410405.
Anderson, M. R. (1997). Determination of a melt onset date for Arctic sea ice regions using passive microwave data. *Annals of Glaciology*, *25*, 382−387.
Barber, D. G., & Hanesiak, J. M. (2004). Meteorological forcing of sea ice concentrations in the southern Beaufort Sea over the period 1979 to 2000. *Journal of Geophysical Research*, *109*, C06014. doi:10.1029/2003JC002027
Barber, D. G., & Nghiem, S. V. (1999). The role of snow on the thermal dependence of backscatter over sea ice. *Journal of Geophysical Research-Oceans*, *104*(C11), 25789−25803.
Barber, D. G., & Yackel, J. J. (1999). The physical, radiative and microwave scattering characteristics of melt ponds on Arctic landfast sea ice. *International Journal of Remote Sensing*, *20*(10), 2069−2090.
Belchansky, G. I., Douglas, D. C., Mordvintsev, I. N., & Platonov, N. G. (2004). Estimating the time of melt onset and freeze onset over Arctic sea-ice area using active and passive microwave data. *Remote Sensing of the Environment*, *92*, 21−39.
Canadian Ice Service Archive Documentation Series (2007). *Regional charts: History, accuracy, and caveats.* http://ice.ec.gc.ca/IA_DOC/cisads_no_001_e.pdf
Carmack, E., MacDonload, R. W., & Jasper, S. (2004). Phytoplankton productivity on the Canadian Shelf of the Beaufort Sea. *Marine Ecology Progress Series*, *277*, 37−50.
Cavalieri, D. J., Gloersen, P., & Campbell, W. J. (1984). Determination of sea ice parameters with the Nimbus 7 SMMR. *Journal of Geophysical Research*, *89*(D4), 5355−5369.
Cavalieri, D., Parkinson, C., Gloersen, P., & Zwally, H. J. (2008). *Sea ice concentrations from Nimbus-7 SMMR and DMSP SSM/I passive microwave data, 1979–2007.*Boulder, Colorado: National Snow and Ice Data Center http://nsidc.org/data/nsidc-0051.html
CIS (2002). Sea ice climatic atlas — Northern Canadian Waters 1971 to 2000. Ottawa: C. I. Service.
Comiso, J. C., Cavalieri, D. J., & Markus, T. (2003). Sea ice concentration, ice temperature, and snow depth using AMSR-E data. *IEEE Transactions on Geoscience and Remote Sensing*, *41*(2), 243−252.
Comiso, J. C. D. J., Cavalieri, D. J., Parkinson, C. L., & Gloerson, P. (1997). Passive microwave algorithms for sea ice concentration: A comparison of two techniques. *Remote Sensing of Environment*, *60*, 357−384.
Comiso, J. C., & Parkinson, C. L. (2008). Arctic sea ice parameters from AMSR-E data using two techniques and comparisons with sea ice from SSM/I. *Journal of Geophysical Research*, *113*, C02S05. doi:10.1029/2007JC004255
Curry, J. A., Schramn, J. L., & Ebert, E. E. (1995). Sea ice-albedo climate feedback mechanism. *Journal of Climate*, *8*, 240−247.
Drinkwater, M. R. (1989). LIMEX '87 ice surface characteristics: Implications for C-band SAR backscatter signatures. *IEEE Transactions on Geoscience and Remote Sensing*, *27*, 501−513.
Drobot, S. D., & Anderson, M. R. (2001). An improved method for determining snow melt-onset dates over Arctic sea-ice using scanning multichannel microwave radiometer and Special Sensor Microwave/Imager data. *Journal of Geophysical Research*, *106*(D20), 24033−24049.
Dunbar, M. (1969). The geographical position of the North Water. *Arctic*, *22*, 438−441.
Early, D. S., & Long, D. G. (2001). Image reconstruction and enhanced resolution imaging from irregular samples. *IEEE Transactions on Geoscience and Remote Sensing*, *39*(2), 291−302.
Eppler, D. T., Farmer, L. D., Lohanick, A. W., Anderson, M. R., Cavalieri, D. J., Comiso, J., Gloersen, P., Garrity, C., Grenfell, T. C., Hallikaninen, M., Maslanik, J., Mätzler, C., Melloh, R. A., Rubinstein, I., & Swift, C. T. (1992). Passive microwave signatures of sea ice. Chapter 4. In F. D. Carsey (Ed.), *Microwave remote sensing of sea iceGeophysical Monograph*, *68*. (pp. 47−68) : American Geophysical Union.
Grenfell, T. C., & Lohanick, A. W. (1985). Temporal variations of the microwave signatures of sea ice during the late spring and early summer near Mould Bay NWT. *Journal of Geophysical Research*, *90*, 5063−5074.
Gunn, B. (2007). *Temporal resolution enhancement for AMSR images.* MERS Technical Report # MERS 07-02, ECEN Department Report # TR-L130-07.02. Brigham Young University: Microwave Earth Remote Sensing (MERS) Laboratory.
Haarpainter, J., & Spreen, G. (2007). Use of enhanced-resolution QuikSCAT/SeaWinds Data for operational ice services and climate research: Sea ice edge, type, concentration, and drift. *IEEE Transactions of Geoscience and Remote Sensing*, *45*(10), 3131−3137.
Haarpaintner, J., Tonboe, R. T., Long, D. G., & VanWoert, M. L. (2004). Automatic detection and validity of the sea ice edge: An application of enhanced resolution QuikScat/SeaWinds data. *IEEE Transactions of Geoscience and Remote Sensing*, *42*(7), 1433−1443.
Howell, S. E. L., Duguay, C. R., & Markus, T. (2009). Sea ice conditions and melt season duration variability within the Canadian Arctic Archipelago: 1979–2008. *Geophysical Research Letters*, *36*, L10502. doi:10.1029/2009GL037681
Howell, S. E. L., Tivy, A., Yackel, J. J., Else, B. G. T., & Duguay, C. R. (2008). Changing sea ice melt parameters in the Canadian Arctic Archipelago: Implications for the future presence of multiyear ice. *Journal of Geophysical Research*, *113*, C09030. doi:10.1029/2008JC004730
Howell, S. E. L., Yackel, J. J., De Abreu, R. A., Geldsetzer, T., & Breneman, C. (2005). On the utility of SeaWinds/QuikSCAT for the estimation of the thermodynamic state of first-year sea ice. *IEEE Transactions on Geoscience and Remote Sensing*, *43*(6), 1338−1350.
Kaufman, D. S., Schneider, D. P., McKay, N. P., Ammann, C. M., Bradley, R. S., Briffa, K. R., Miller, G. H., Otto-Bliesner, B. L., Overpeck, J. T., & Vinther, B.Arctic Lakes 2 k Project Members. (2009). Recent warming reverses long-term Arctic cooling. *Science*, *325*, 1236−1239. doi:10.1126/science.1173983
Kwok, R., Cunningham, G. F., & Nghiem, S. V. (2003). A study of melt onset in RADARSAT SAR imagery. *Journal of Geophysical Research*, *108*(C11), 3363. doi:10.1029/2002JC001363
Long, D. G., & Daum, D. L. (1998). Spatial resolution enhancement of SSM/I data. *IEEE Transactions on Geoscience and Remote Sensing*, *36*(2), 407−417.
Long, D. G., Hardin, P. J., & Whitling, P. T. (1993). Resolution enhancement of spaceborne scatterometer data. *IEEE Transactions in Geoscience and Remote Sensing*, *31*(3), 700−715.
Markus, T., Powell, D., & Wang, J. (2006). Sensitivity of passive microwave snow depth retrievals to weather effects and snow evolution. *IEEE Transactions on Geoscience and Remote Sensing*, *44*(1), 68−77.
Markus, T., Stroeve, J. C., & Miller, J. (2009). Recent changes in Arctic sea ice melt onset, freeze-up, and melt season length. *Journal of Geophysical Research*. doi:10.1029/2009JC005436
Mätzler, C. (1992). Ground-based observations of atmospheric radiation at 5, 10, 21, 35, and 94 GHz. *Radio Science*, *27*(3), 403−415. doi:10.1029/91RS03052
Melling, H. (2002). Sea ice of the northern Canadian Arctic Archipelago. *Journal of Geophysical Research*, *107*(C11), 3181. doi:10.1029/2001JC001102
Miller, D. H. (1981). *Energy at the surface of the Earth: An introduction to the energetics of ecosystems.* New York: Academic Press.
Nghiem, S. V., Chao, Y., Neumann, G., Li, P., Perovich, D. K., Street, T., & Clemente-Colón, P. (2006). Depletion of perennial sea ice in the East Arctic Ocean. *Geophysical Research Letters*, *33*, L17501. doi:10.1029/2006GL027198
Onstott, R. G. (1992). SAR and scatterometer signatures of sea ice. In F. Carsey (Ed.), *Microwave remote sensing of sea iceAmerican Geophysical Union, Geophysical Monograph*, *Vol. 68*. (pp. 73−104) Chapter 5.
Perovich, D. K., Nghiem, S. V., Markus, T., & Schweiger, A. (2007). Seasonal evolution and interannual variability of the local solar energy absorbed by the Arctic sea ice–ocean system. *Journal of Geophysical Research*, *112*, C03005. doi:10.1029/2006JC003558
Perovich, D. K., Richter-Menge, J. A., Jones, K. F., & Light, B. (2008). Sunlight, water, and ice: Extreme Arctic sea ice melt during the summer of 2007. *Geophysical Research Letters*, *35*, L11501. doi:10.1029/2008GL034007

Serreze, M. C., Barrett, A. P., Stroeve, J. C., Kindig, D. N., & Holland, M. M. (2009). The emergence of surface-based Arctic amplification. *The Cryosphere*, *3*, 11−19.

Serreze, M. C., Holland, M. M., & Stroeve, J. (2007). Perspectives on the Arctic's shrinking sea-ice cover. *Science*, *316*, 1533−1536.

Steele, M., Ermold, W., & Zhang, J. (2008). Arctic Ocean surface warming trends over the past 100 years. *Geophysical Research Letters*, *35*, L02614. doi:10.1029/2007GL031651

Stroeve, J. C., Markus, T., Meier, W. N., & Miller, J. (2006). Recent changes in Arctic melt season. *Annals of Glaciology*, *44*, 367−374.

Stroeve, J., Serreze, M., Drobot, S., Gearheard, S., Holland, M., Maslanik, J., Meier, W., & Scambos, T. (2008). Arctic sea ice extent plummets in 2007. *EOS. Transactions of the American Geophysical Union*, *89*(2). doi:10.1029/2008EO020001

Tedesco, M., & Wang, J. (2006). Atmospheric correction of AMSR-E brightness temperatures for dry snow cover mapping. *IEEE Geoscience and Remote Sensing Letters*, *3*(3), 320−324.

Ulaby, F. T., Moore, R. E., & Fung, A. K. (1986). *Microwave remote sensing: Active and passive*.MA: Addison-Wesley Publishing Company Vols. 1, 2 and 3.

Wang, L., Derksen, C., & Brown, R. (2008). Detection of pan-Arctic terrestrial snowmelt from QuikSCAT, 2000–2005. *Remote Sensing of Environment*, *112*, 3794−3805. doi:10.1016/j.rse.2008.05.017

Wang, X., & Key, J. R. (2005). Arctic surface, cloud, and radiation properties based on the AVHRR Polar Pathfinder dataset. Part I: Spatial and temporal characteristics. *Journal of Climate*, *18*, 2575−2593.

Winebrenner, D. P., Holt, B., & Nelson, E. D. (1996). Observation of autumn freeze-up in the Beaufort and Chukchi Seas using the ERS 1 synthetic aperture radar. *Journal of Geophysical Research*, *101*(C7), 16401−16419.

Winebrenner, D. P., Nelson, E. D., Colony, R., & West, R. D. (1994). Observation of melt onset on multiyear Arctic sea ice using ERS-1 synthetic aperture radar. *Journal of Geophysical Research*, *99*, 22425−22441.

Winton, M. (2006). Amplified Arctic climate change: What does surface albedo feedback have to do with it? *Geophysical Research Letters*, *33*, L03701. doi:10.1029/2005GL025244

Yackel, J. J., & Barber, D. G. (2000). Melt ponds on sea ice in the Canadian Arctic Archipelago. Part 2. On the use of RADARSAT-1 synthetic aperture radar for geophysical inversion. *Journal of Geophysical Research-Oceans*, *105*(C9), 22061−22070.

Yackel, J. J., Barber, D. G., & Papakyriakou, T. N. (2001). On the estimation of spring melt in the north water polynya using RADARSAT-1. *Atmosphere-Ocean*, *39*, 195−208.

Yu, P., Clausi, D. A., & Howell, S. E. L. (2009). Fusing AMSR-E and QuikSCAT imagery for improved sea ice recognition. *IEEE Transactions on Geoscience and Remote Sensing*, *47*(7), 1980−1990. doi:10.1109/TGRS.2009.2013632

Yueh, S. H., Kwok, R., Lou, S., & Tsai, W. (1997). Sea ice identification using dual-polarized Ku-band scatterometer data. *IEEE Transactions on Geoscience and Remote Sensing*, *35*, 560−569.